Cell Reports
Physical Science

Article

Next-generation battery heat shield based on lithium nitrate molten-salt phase-change material for thermal-runaway prevention

Graphical abstract

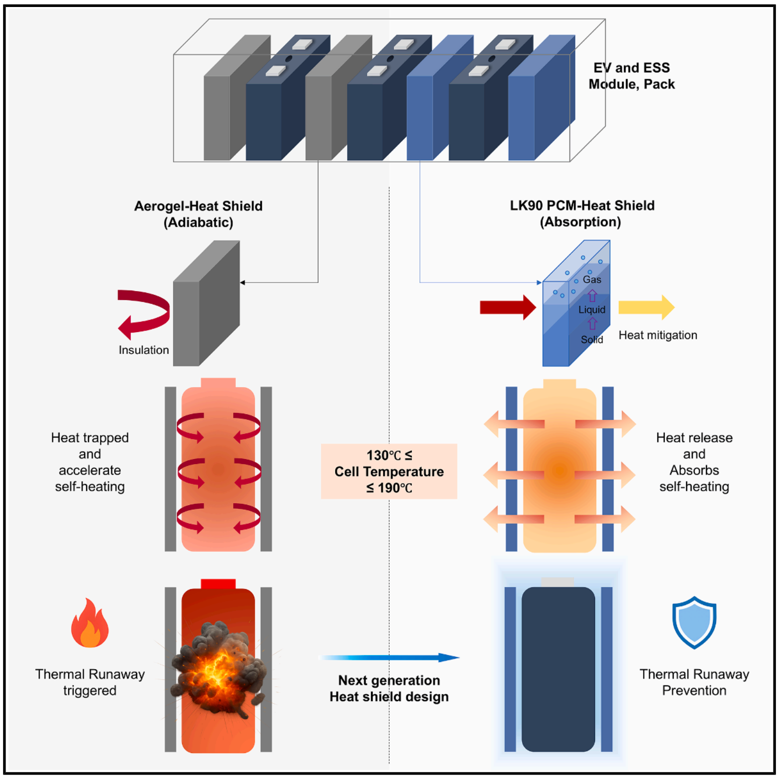

Highlights

- Introduces molten-salt PCM heat shield with novel compositions for TR prevention
- PCM heat shield delays separator melting by 500 s vs. silica aerogel sheet
- Ensures passive protection across critical 130°C–190°C TR window
- Meets key safety standards, including UL 9540A and UN 38.3

Authors

Jae-Yeon Choi, Min-Hong Park,
Jack J. Yoh

Correspondence

jjyoh@snu.ac.kr

In brief

Lithium nitrate-rich non-eutectic molten salt functions as a phase-change-material heat shield that melts within the critical thermal runaway window and prevents propagation. Choi et al. demonstrate a passive high-latent-heat-capacity solution that replaces aerogel and enhances safety in next-generation EV battery packs.

Choi et al., 2025, Cell Reports Physical Science 6, 102920

https://doi.org/10.1016/j.xcrp.2025.102920

CellPress

Cell Reports
Physical Science

CellPress
OPEN ACCESS

Article

Next-generation battery heat shield based on lithium nitrate molten-salt phase-change material for thermal-runaway prevention

Jae-Yeon Choi,[1,2] **Min-Hong Park,**[1,2] **and Jack J. Yoh**[1,3,*]
[1]Department of Aerospace Engineering, Seoul National University, Seoul 08826, South Korea
[2]These authors contributed equally
[3]Lead contact
*Correspondence: jjyoh@snu.ac.kr
https://doi.org/10.1016/j.xcrp.2025.102920

SUMMARY

Thermal runaway (TR) and TR propagation (TRP) in lithium-ion batteries (LIBs) pose critical safety risks. Here, we report a dual-function heat shield based on a molten-salt phase-change material (PCM) that concurrently manages TR and prevents TRP. The optimized $LiNO_3$-KCl blend (LK90) begins melting at 142°C and absorbs 308 J g^{-1} of latent heat within the critical 130°C–190°C safety window. Encapsulated in a stainless-steel pouch, the PCM heat shield outperforms a commercial aerogel sheet of equal thickness, delaying the rise of critical temperatures by more than 500 s in rapid heating tests. During a 90-min thermal soak at 130°C, it successfully prevents a fully charged cell from entering TR. This work provides a passive single layer that can be retrofitted into existing electric vehicle modules, enhancing safety without added volume or active control.

INTRODUCTION

Lithium-ion batteries (LIBs) are indispensable in applications ranging from portable electronics to electric vehicles (EVs), thanks to their high energy density and reliable electrochemical performance.[1–3] For pack-level use, numerous cells are assembled in close proximity to satisfy demanding energy and power requirements,[4] a configuration that intensifies thermal safety concerns.[5–7]

Thermal runaway (TR) is an uncontrolled exothermic sequence that releases flames, pressure, and flammable gases.[8–11] It can be triggered by mechanical impact or penetration,[12,13] electrical abuse such as over-charge or internal short circuit,[14,15] and external heating.[16,17] Interfacial breakdowns, gas evolution, and redox heat reinforce each other in a positive-feedback loop.[18,19] Figure 1 highlights three temperature landmarks: solid-electrolyte-interphase decomposition starts near 80°C, rapid self-heating begins above about 130°C, and ceramic-coated separators melt close to 190°C, after which flames are likely to appear.[20–22] The interval from 130°C to 190°C is therefore a TR-management window, whereas temperatures beyond 190°C demand a propagation heat shield.

TR propagation (TRP), in which a failing cell ignites its neighbors, is equally critical.[23,24] Flame temperatures in high-nickel cathodes can exceed 1,100°C, overwhelming conventional safeguards.[25] Most battery packs position a thin insulating sheet between neighboring cells. Any such inter-cell spacer is termed a heat shield in this study. Commercial aerogel sheets perform this duty by slowing the heat conduction, but they store almost no latent heat and cannot buffer the 130°C–190°C TR window or halt propagation once the temperature climbs above 190°C. A single material that can fulfill both roles has remained unknown and is still missing.

Silica aerogel sheets, hereafter aerogel heat shields (aerogel-HSs), are widely installed as intercell spacers because their thermal conductivity is about 0.02 W m^{-1} K^{-1} and their density is below 0.12 g cm^{-3}.[26] They act as insulation and store less than 2 J g^{-1} of latent heat, so they cannot buffer a 130°C–190°C management window. This limitation motivates phase-change materials (PCMs) that absorb heat while melting in the TR-management window and, once molten, also limit heat transfer during TRP.

Battery PCMs are commonly grouped into organic, inorganic, and composite classes. Organic PCMs such as paraffins are easy to process and cycle well, but they melt below the abuse window, have low thermal conductivity, and can be flammable, so they do not protect against both TR and TRP.[27] Mixed molten-salt PCMs allow composition-based tuning of melting onset and latent heat; nitrates contribute high latent heat and chlorides help adjust the melting point. These mixtures are nonflammable, typically melt within 130°C–300°C, deliver 200 J g^{-1} of latent heat, and have moderate thermal conductivity on the order of 0.6 W m^{-1} K^{-1}.[28] Composite PCMs with expanded graphite or ceramic scaffolds improve shape stability and heat spreading, but they dilute latent heat and add mass. The remaining gap is a thin single layer that activates inside the safety window and absorbs enough heat to manage both TR and TRP; this motivates the $LiNO_3$-rich strategy pursued here.

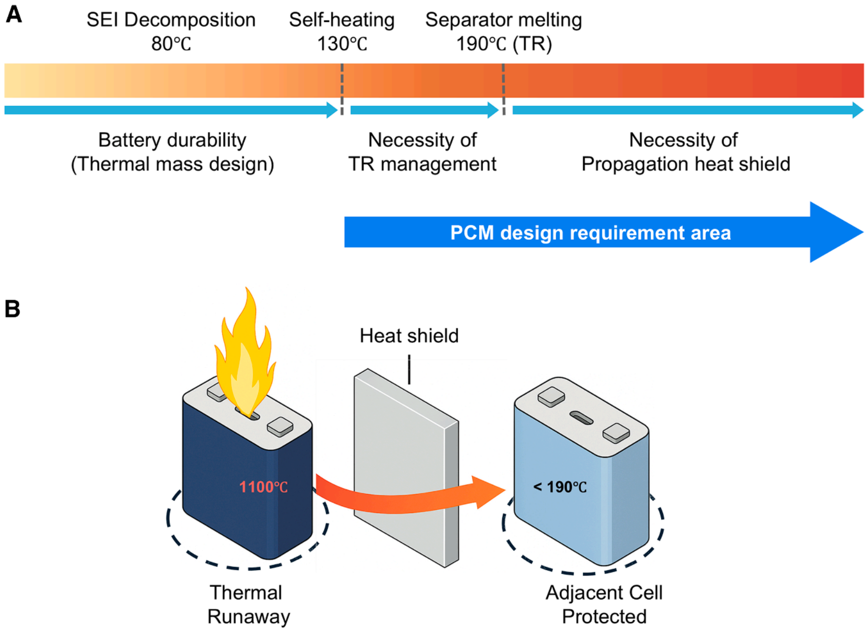

Figure 1. Temperature window of TR and schematic of a PCM-HS

(A) Temperature landmarks during lithium-ion cell abuse.

(B) Conceptual schematic of a PCM-HS preventing a cell in TR from raising its neighbor above 190°C.

Recent studies report that pure PCMs often delay TRP,[29] while coupling a PCM with an auxiliary flow path can further suppress propagation under aggressive loads.[30,31] This supports optimizing latent heat and onset first and then considering hybridization only where needed. For example, a serpentine composite PCM plate combined with forced-air convection reduced peak temperatures and improved thermal uniformity in a cylindrical cell module, but it added mass and complexity compared with a single passive layer.[32,33] Composite PCMs with oriented carbon fibers raise effective thermal conductivity while retaining useful latent heat, although some dilution of energy density is typical and must be balanced against weight and volume targets.[34] Demand for compact and nonflammable PCMs is rising across EV battery safety; stationary energy storage and grid thermal storage; building heating, ventilation, and air conditioning (HVAC); electronics cooling; and aerospace, where passive buffering within a narrow window is preferred over added hardware. Table 1 summarizes representative options in this focused space and sets the targets for our $LiNO_3$-based selection.

Among various candidates, lithium nitrate ($LiNO_3$) is especially promising. It offers one of the highest latent heats, typically above 200.0 J g^{-1}, exhibits excellent thermal stability up to 500°C, has a suitable intrinsic onset temperature, and remains chemically stable with only moderate corrosivity. These characteristics make it a strong foundation for a single layer that fulfills both TR-management and propagation heat-shield roles.[41] Furthermore, the addition of potassium chloride (KCl) to $LiNO_3$ has been shown in previous research to effectively lower the mixture's melting point, making $LiNO_3$-KCl systems particularly interesting for achieving the desired thermal properties within the TR-management window.

To identify an optimal $LiNO_3$-based PCM, 12 formulations were prepared and screened by differential scanning calorimetry (DSC). Three parent systems were examined. $LiNO_3$:$NaNO_3$:KCl (LNK) was prepared at its eutectic ratio 55.4:4.5:40.1 wt %. $LiNO_3$:KCl (LK) started from the eutectic 58.1:41.9 wt %. $LiNO_3$:NaCl (LNA) started from the eutectic 87:13 wt %.[42–44] In each system, the $LiNO_3$ fraction was then changed. In the LK series, the eutectic shows an onset temperature of 133°C and a latent heat of 212 J g^{-1}, while a non-eutectic 90:10 wt % blend, referred to as LK90, raises the onset to 142°C and the latent heat to 308 J g^{-1}. LNA shows only modest latent-heat changes when $LiNO_3$ is raised, and LNK behaves in between. Because earlier work focused on eutectic mixtures, LK90 represents a new $LiNO_3$-KCl formulation deliberately tuned for the TR-management window yet still capable of acting as a heat shield beyond 190°C.

Production EV modules apply several kN of compression to maintain cell alignment and to limit swelling. Thus, the same pressure is recreated in every thermal test reported in this research, as detailed in the methods section.

LK90, sealed in stainless-steel (SUS) pouches, was evaluated by four complementary experiments: (1) DSC confirmed onset and latent heat, (2) a film-heater ramp test measured delay time and real-time latent uptake under a rising heat pulse, (3) a constant-flux hot-plate dwell quantified total heat absorbed below 190°C, and (4) a 130°C oven soak, extended to 90 min, was performed to satisfy the thermal stability criteria demanded by international battery-safety certifications and to quantify self-heating suppression under those conditions. Aerogel-HS served as the industry reference in (2) film-heater test and (4) thermal stability test.

Prior studies on PCM-based battery cooling have mainly targeted routine charge and discharge at low temperature. These approaches slow conduction but rarely prevent TR or its propagation because they melt far below the abuse window and store little latent heat.[45] What is missing is a single passive layer that activates inside the safety window and absorbs enough heat to stop both the onset of runaway and the spread to adjacent cells.

Here, we present a dual-function heat-shield design using an $LiNO_3$ and potassium chloride mixture (LK90) that strategically moves away from the eutectic point to maximize latent heat. This approach directly addresses the critical 130°C–190°C TR-management window. Encapsulated in a stainless-steel pouch, the LK90 heat shield significantly outperforms a commercial aerogel sheet: in a film-heater ramp test, it delays critical temperature rise by over 500 s, and, in a 90-min thermal soak at 130°C, it successfully prevents a fully charged cell from entering TR while

Table 1. Thermophysical comparison that motivates the choice of a $LiNO_3$-based molten-salt PCM

Family	Representative composition	Melting T/°C	ΔH/J g^{-1}	Fit for battery?	Key reason	Reference
Insulation baseline	silica aerogel sheet (aerogel-HS)	–	<2	yes	blocks conduction; no latent buffer	Xiong et al.[35]
Organic PCM	*n*-octadecane ($C_{18}H_{38}$)	28	236	no	high ΔH but melts below 130°C; flammable	Chen et al.[36]
Chloride	$MgCl_2$-NaCl (43.1/57.9 wt %)	459	333	no	melts far above 190°C	Myers and Goswami[37]
Carbonate	Na_2CO_3-Li_2CO_3 (58/42 wt %)	498	330	no	melts far above 190°C	Jiang et al.[38]
Mixed nitrate (reference)	$NaNO_3$-KNO_3 (60/40 wt %, Solar salt)	220	142	no	industrial heat storage benchmark	Orozco et al.[39]
Low-melt nitrate	$LiNO_3$-$NaNO_3$-KNO_3 (30/18/52 wt %)	123	140	no	meets melting window but ΔH still modest	Pereira da Cunha and Eames[28]
Li-nitrate base salt	pure $LiNO_3$	254	372	no	highest latent heat among nitrates; nonflammable and non-corrosive	Alario et al.[40]
Li-nitrate + halide	$LiNO_3$-$NaNO_3$-KCl (55.4/4.5/40.1 wt %)	145 (onset)	159	no	onset acceptable; ΔH below 200 J g^{-1}	this work
Li-nitrate + halide	$LiNO_3$-KCl (58.1/41.9 wt %)	133 (onset)	212	yes	window 130°C–190°C & ΔH $\geq$ 200 J g^{-1}	this work
Li-nitrate + halide	$LiNO_3$-NaCl (87/13 wt %)	204 (onset)	327	no	excellent ΔH but $T_m > 190$°C	this work
Li-nitrate tuned (this work)	LK90 $LiNO_3$–KCl (90/10)	142 (onset)	308	yes	onset & ΔH tuned for TR window	this work

Compositions are in wt % unless otherwise stated. ΔH $\geq$ 200 J g^{-1} and 130 $\leq T_m \leq$ 190°C are considered "yes."

the aerogel assembly fails. By integrating materials selection, encapsulation, and validation against industry-relevant protocols, this work establishes a framework for designing passive, single-layer phase-change heat shields that effectively prevent both TR and its propagation.

RESULTS AND DISCUSSION

DSC screening identifies LK90 as the optimal composition

DSC analysis was carried out on four compositions for each parent salt system. Each set comprised the eutectic and three non-eutectic variants prepared with $LiNO_3$ mass fractions of 70, 80, and 90 wt %. For every formulation, the onset temperature, defined by the baseline-intersection method, and the latent heat of fusion were extracted from scans recorded at 20°C min^{-1}. Five repeats per sample yielded an onset scatter of ±3°C and a latent-heat repeatability of ±7%. Table 2 compiles the numerical results.

Figure 2A confirms that changing the $LiNO_3$ fraction shifts the onset temperature by only a few degrees in every system, which keeps the activation window centered near 130°C except LNA systems. Figure 2B reveals a different trend in latent heat. The LNK and LK series exhibit a monotonic rise as $LiNO_3$ increases, whereas the LNA series remains flat because its eutectic is already $LiNO_3$ rich.

Within the LK family, the 90 wt % mixture (LK90) combines the promising onset temperature of about 142°C with the highest enthalpy of fusion, 308 J g^{-1}, which is 45% higher than the eutectic. This balance of activation temperature and energy density makes LK90 the prime candidate for TR management and propagation shielding, making subsequent pouch studies focused on this composition.

Figure 2C overlays DSC curves of the eutectic LK and LK90. LK90 initiates heat uptake just above 140°C and continues to absorb until roughly 260°C. A battery pack is designed to tolerate temperatures up to about 130°C without damage, so setting the PCM onset near 140°C prevents parasitic heat storage during normal operation yet responds immediately once cells exceed their safe limit. The broad 120°C endothermic span acts as a thermal buffer: the pouch face in contact with a runaway cell climbs rapidly, while the inner PCM remains cooler and draws heat away. Model calculations in next section show that this buffer keeps the opposite face of the pouch below the 190°C propagation threshold, thereby blocking TRP without resorting to overengineering the latent-heat capacity.

Table 2. Onset temperature and latent heat of $LiNO_3$-based eutectic (eut.) and non-eutectic PCM mixtures

System	$LiNO_3$/wt %	Onset/°C	Latent heat/J g^{-1}
LNK	55.4 (eut.)	145	159
LNK70	70	137	207
LNK80	80	150	246
LNK90	90	159	299
LK	58.1 (eut.)	133	212
LK70	70	130	269
LK80	80	130	277
LK90	90	142	308
LNA	87 (eut.)	204	327
LNA70	70	201	235
LNA80	80	209	288
LNA90	90	203	319

In practice, heat flux varies from cell to cell. Because the LK90 plateau covers almost the full 140°C–260°C interval, the material continues to absorb energy even when one cell runs hundreds of degrees hotter than its neighbor, providing a margin against spatial non-uniformity while preserving pack efficiency.

Film-heater ramp test shows extended protection over aerogel

The stepped-voltage protocol imposes an identical heat-flux profile on all heat-shield specimens. Figure 3 compares the thermal response of the silica aerogel-HS and the PCM heat shield (PCM-HS). Figure 3A overlays front- and back-side temperatures for both shields (solid = front, dashed = back). Figure 3B plots the back-side heating rate, dT_{back}/dt, versus the average laminate temperature, T_{avg}, for the PCM-HS; the gray band in Figure 3B spans 140°C–260°C and corresponds to the latent-heat window determined by DSC. Traces are plotted to 1,150 s, the last instant before electrical pick-up distorts the thermocouple signals.

The electrical power delivered to the film heater is

$$P_{in}(t) \;=\; \eta V(t) I(t), \eta = 0.70. \qquad \text{(Equation 1)}$$

Surface losses occur mainly by natural convection and edge radiation because both faces are clamped between insulation boards. They are estimated by

$$P_{loss}(t) = h_{\parallel} A_{\parallel}\left[T_{avg}(t) - T_{air}\right] + \varepsilon\sigma A_{\parallel}\left[\left(T_{avg}+273\right)^4 - \left(T_{air}+273\right)^4\right], \qquad \text{(Equation 2)}$$

where $h_{\parallel} = 38\ Wm^{-2}K^{-1}, A_{\parallel} = 8.49 \times 10^{-4} m^2$, $\varepsilon = 0.50$ for the aerogel sheet and 0.30 for the SUS pouch, and $T_{avg} = (T_{front} + T_{back})/2$. Direct radiation from the large faces is blocked by the insulation boards and is therefore omitted. Sensible storage follows

$$P_{sens}(t) \;=\; m_{tot} C_{p,avg} \frac{dT_{avg}}{dt}, \qquad \text{(Equation 3)}$$

and the instantaneous endothermic rate follows from an energy balance

$$P_{endo}(t) \;=\; P_{in} \;-\; P_{sens} \;-\; P_{loss}. \qquad \text{(Equation 4)}$$

Time integration provides the cumulative energies summarized in Table 3.

In Figure 3A, the two front-side curves rise together for the first 200 s. Once the heater exceeds 20 V, the aerogel-HS accelerates sharply, surpassing 550°C at 1,150 s. The PCM-HS climbs more slowly and remains below 390°C. The back-side curves coincide up to about 800 s; thereafter, the PCM-HS bends, signaling the start of latent-heat absorption, and stays below 160°C. aerogel-HS crosses the 190°C propagation limit at 1,031 s; a linear extrapolation suggests that PCM-HS would need about 1,500 s to reach the same temperature.

Figure 3B corroborates this trend. The aerogel-HS derivative rises steadily to 0.70°C s^{-1}, whereas the PCM-HS derivative dips to 0.12°C s^{-1} within the gray band. Over the same interval, the PCM-HS T_{avg} traverses 140°C–260°C, matching the latent-heat uptake seen in the DSC scan. The average temperature of aerogel-HS is omitted because it rises monotonically and conveys no information beyond the front- and back-side curves already shown in Figure 3A.

Only the front face is heated, so $T_{front} - T_{back}$ exceeds 200°C by the end of the ramp. Even with this large gradient, the simple average T_{avg} is a useful proxy for the bulk PCM temperature. Latent melting spreads the heat almost uniformly inside the 3-mm layer, and the moment when T_{avg} crosses 140°C and 260°C coincides with the trough in dT_{back}/dt in Figure 3B. The match confirms that the average marks the beginning and end of the latent-heat uptake window for the geometry tested here.

LK90 moderates the front-side temperature rise from the outset and, once its phase transition initiates, restricts the back-side increase as well. The trace never forms a true plateau because the heater power keeps climbing, yet the clear flattening inside the latent-heat window shows that the salt is still absorbing heat. The enthalpy recovered *in situ*, 309 J g^{-1}, matches the DSC value to within 1%. aerogel-HS, by contrast, stores only sensible heat: almost all input power leaves through the exposed edges and Q_{latent} is effectively zero. Consequently, PCM-HS keeps its back side below the 190°C propagation limit, whereas the conductive aerogel-HS cannot.

Constant-flux hot-plate dwell confirms heat absorption within the safety window

The dynamic ramp proved that the PCM-HS slows a rapidly rising heat source. A complementary test evaluated its ability to absorb a steady flux. One face of the PCM-HS was pressed against a flat, ceramic-coated plate maintained at 250°C, while the opposite face was insulated on the back with an insulation board and fitted with type-K thermocouples. A 10-kg load ensured intimate contact and removed air gaps. Temperature was recorded at 10 Hz and then smoothed with a Savitzky-Golay filter that used a 401-point window, followed by a 101-point moving average.

Figure 4A displays the back-side temperature. Vertical gray bars mark 130°C and 190°C, the separator safety window identified earlier. The back side reaches the lower limit after 520 s. During the next 940 s, the curve bends steadily and climbs only 60°C.

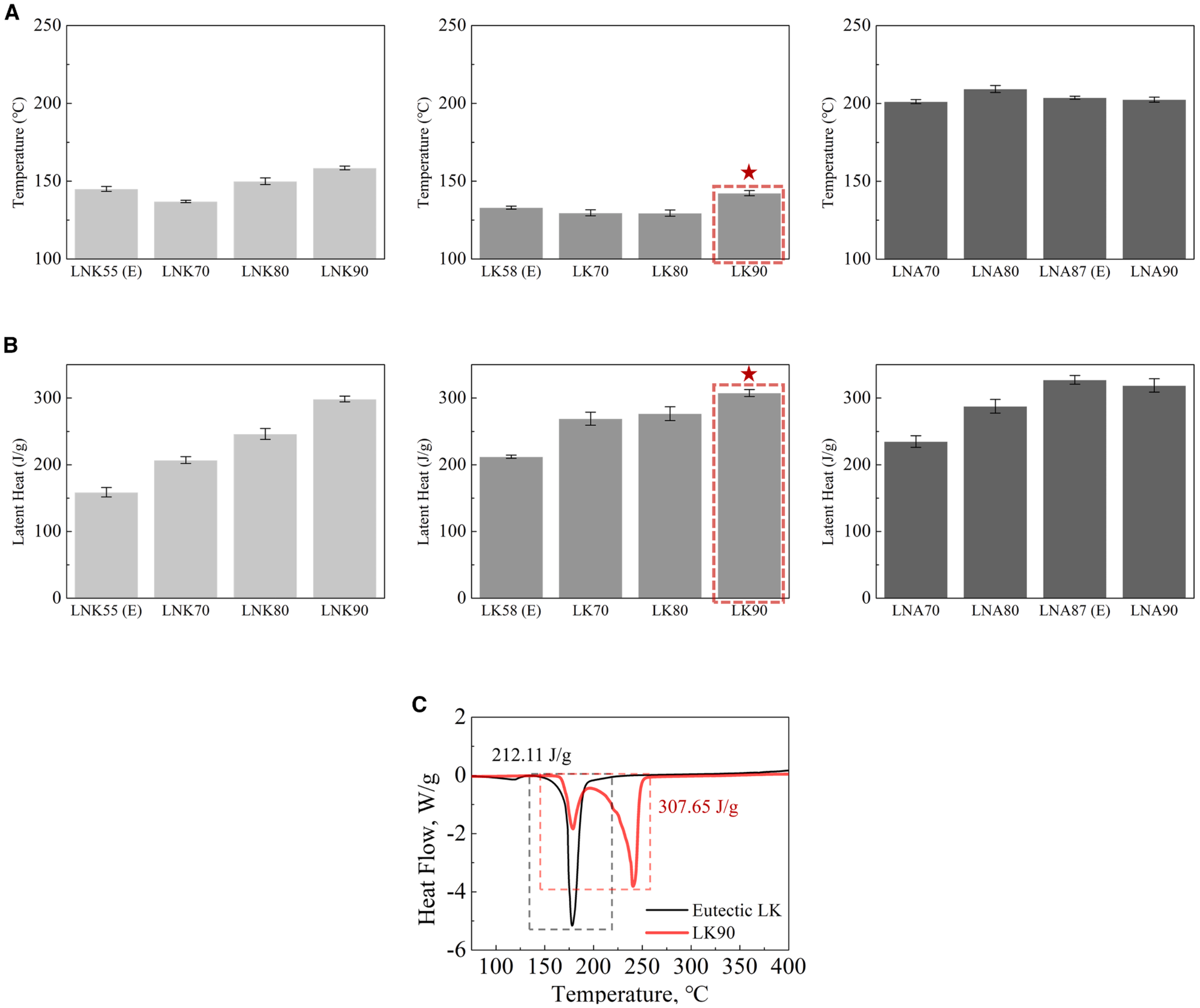

Figure 2. DSC screening of $LiNO_3$-based PCM systems

(A) Onset temperatures of LNK, LK, and LNA series at varying $LiNO_3$ fractions (mean ± SD, $n = 5$; onset SD = 1.4°C–1.7°C across compositions).

(B) Latent heat of fusion for the same systems (mean ± SD, $n = 5$; latent-heat SD = 3.3%–3.9% of the mean).

(C) Representative DSC scans recorded at 20°C min^{-1}, which show the broader endothermic plateau of LK90 relative to the eutectic.

Figure 4B plots the heating rate of the back side. Within the shaded band, the average temperature $(T_{front} + T_{back})/2$ stays between 140°C and 260°C. Inside this band, the derivative falls to -0.001°C s^{-1}, matching the latent-heat interval seen in DSC.

At 2,400 s the back side reaches 220°C, which exceeds the separator melt threshold. The heating rate, however, stays below 0.1°C s^{-1}. Latent absorption is largely exhausted, and the residual rise is driven mainly by sensible heating. Quantitative markers are summarized in Table 4.

Oven-soak thermal-stability test demonstrates prevention of TR

The ramp test proved that a PCM-HS postpones a sudden heat surge, and the constant-flux test showed that the delay persists when one face sits at 250°C. The final step examines whether the PCM-HS can stop a cell from igniting while environment temperature remains at 130°C for 90 min.

A mini prismatic cell with a 90% nickel cathode was installed in two identical stacks. The reference stack placed an aerogel-HS on both broad faces of the cell. The comparison stack used a PCM-HS in those positions. Each heat shield contacted an aluminum plate that simulated the adjacent cell. Insulation boards and outer aluminum partitions enclosed the assembly, which was clamped with a compressive load representative of production modules. The convection oven rose from ambient to 130°C at 5°C min^{-1} and then held that level for 90 min. Three type-K thermocouples logged one reading per second: T_{center} at the midpoint of the broad face of the cell, T_{side} at the

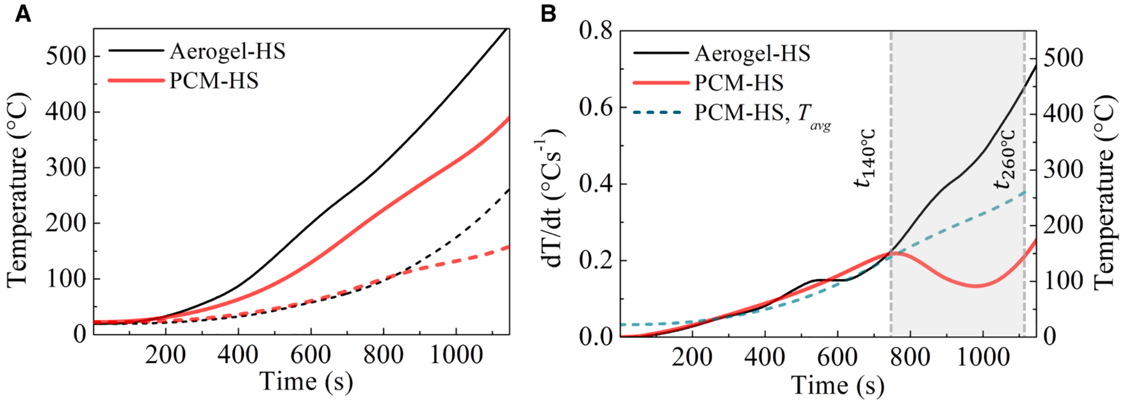

Figure 3. Stepped voltage film-heater ramp test

(A) Front- and back-side temperature of the PCM-HS and the aerogel-HS; solid lines = front, dashed lines = back.

(B) Back-side heating rate dT_{back}/dt with T_{avg} of PCM-HS. The gray band marks the latent-heat window (140°C–260°C).

midpoint of the narrow face of the cell, and $T_{ambient}$ in the air beside the stack.

Figure 5A shows the aerogel-HS result. T_{center} and T_{side} follow $T_{ambient}$ during the ramp but cross above it at 3,623 s. The difference keeps growing until 5,506 s when T_{center} passes 190°C and battery TR begins. Core temperature climbs beyond 800°C a few seconds later. The inset enlarges the interval from 3,000 to 5,000 s where battery self-heating accelerates.

Figure 5B gives the PCM-HS result. T_{center} drifts above $T_{ambient}$ just before 3,857 s and then settles near 131°C. T_{side} stays about 1°C cooler. No gas release or flame appears during the entire dwell. The inset confirms that every trace remains grouped while the oven holds at 130°C.

Figure 5C plots $\Delta T = T_{center} - T_{ambient}$ for both stacks. The aerogel-HS trace rises steadily, surpasses 35°C at 5,414 s, and continues upward until battery TR. In contrast, the PCM-HS trace tops out at only 4°C at 6,477 s and then declines, showing that the latent melting of LK90 removes almost all internally generated heat.

When the oven was opened and the clamp released, the cell next to the PCM-HS appeared visibly swollen. This swelling confirms that self-heating continued under confinement, while the molten-salt shield absorbed the heat and limited the surface temperature during the 130°C soak.

These three experiments paint a coherent picture. The power ramp quantifies the delay against a fast surge, and the hot-plate test measures sustained buffering under a fixed load. The stability test shows that a single 3-mm PCM-HS keeps a cell below the separator limit for the full 90 min required by transport regulations. This protection holds even when the module environment remains at 130°C. A conduction-only aerogel-HS cannot absorb the internal heat, so self-heating escalates and TR follows.

In summary, this study demonstrates that a single thin layer of $LiNO_3$-KCl molten-salt PCM, formulated as LK90 and encapsulated in a stainless-steel pouch, delivers both TR management and propagation shielding. LK90 acts in two stages: below its melting onset it contributes sensible thermal mass, and above 142°C its latent-heat throttles incoming flux up to 260°C, ensuring effective buffering within the 130°C–190°C safety window. This passive layer replaces separate insulators and heat sinks with a single multifunctional component that can be integrated into existing module hardware, offering a practical path toward lighter and safer EVs and energy-storage batteries. Future work will address durability under repeated melting and solidification, corrosion and leakage qualification, detailed thermal property measurements, and full module-scale propagation tests under representative conditions.

METHODS

PCM synthesis and pouch encapsulation

$LiNO_3$ (Samchun Chemicals, ≥99%), sodium nitrate ($NaNO_3$; Junsei Chemical, ≥99%), sodium chloride (NaCl; Samchun Chemicals, ≥99%), and potassium chloride (KCl; Junsei Chemical, ≥99%) were dried in a convection oven at 110°C for 24 h. Each salt was weighed to ±0.1 mg, combined according to the target mass ratios (compositions in Table 2), and thoroughly hand mixed in a sealed polypropylene jar.

To enhance thermal performance, specifically to delay battery TR while suppressing TRP, mixtures were tuned above their eutectic points to raise the latent heat and widen the heat-absorption window. Three parent systems were examined: LNK, LK, and LNA. For each system, the eutectic composition served as a baseline (55.4:4.5:40.1 wt % for LNK, 58.1:41.9 wt % for LK,

Table 3. Quantitative metrics from the stepped-voltage film-heater ramp test

Specimen	$t_{130,back}$ (s)	$t_{190,back}$ (s)	Q_{in} (kJ)	Q_{sens} (kJ)	Q_{loss} (kJ)	Q_{latent} (kJ)	q_{latent} (J g^{-1})
Aerogel-HS	897	1,031	55.2	4.8	50.4	0.0	0.0
PCM-HS	987	>1,200	55.2	14.9	31.4	9.0	309

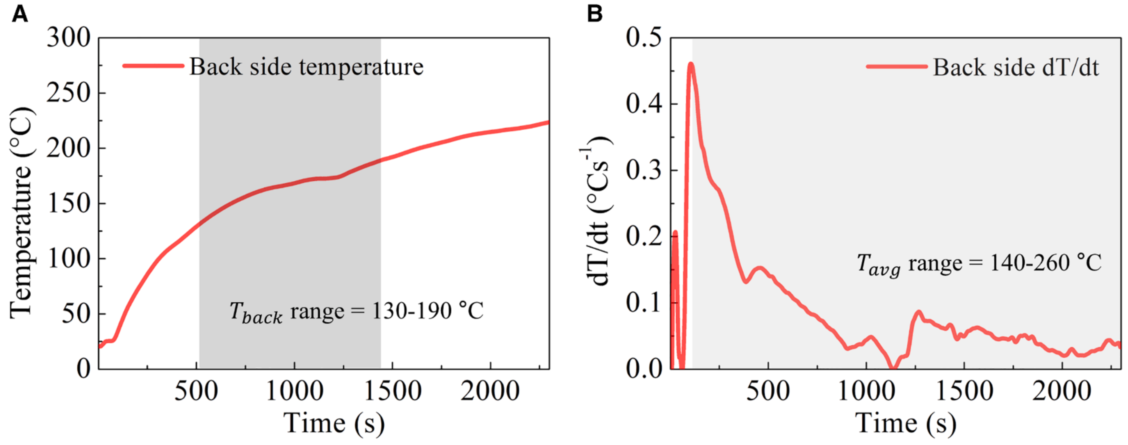

Figure 4. Constant-boundary hot-plate dwell at 250°C

(A) Back-side temperature of the PCM-HS. Gray bars delimit the separator safety window 130°C–190°C.

(B) Back-side heating rate dT/dt. The shaded region marks the LK90 latent-heat range 140°C–260°C identified by DSC.

and 87:13 wt % for LNA); the $LiNO_3$ content was then adjusted stepwise to find a composition that offer a suitable onset temperature and the highest latent heat. LNK and LK were prepared at 70, 80, and 90 wt % $LiNO_3$ in addition to their eutectics, while LNA was prepared at 70, 80, the eutectic 87, and 90 wt % $LiNO_3$. The $LiNO_3$-rich LK90 ($LiNO_3$:KCl = 90:10 wt %) combined an onset of 142°C with a latent heat of 308 J g^{-1} and was selected for further testing.

Each 30-g batch was fused in alumina dishes at 450°C for 30 min (muffle furnace, SH-FU-3MGE) and allowed to furnace cool. The solid cakes were ground (<100 μm) and redried at 110°C for 24 h. Because $LiNO_3$ is strongly hygroscopic, all powder handling took place in a dry atmosphere, and the samples were sealed immediately after drying.

For performance tests, the melt was cast into 3-mm-thick plates, cooled, and radiofrequency (10 kHz, 2 s) sealed between 50-μm stainless-steel (SUS 304) films. A finished pouch weighing 29 g (LK90) + 8 g (SUS) is hereafter termed a PCM-HS. The full preparation route appears in Figure 6A.

Differential scanning calorimetry

DSC analysis was used to characterize the thermal properties of the PCM mixtures described above. Samples included the eutectic compositions of LNK, LK, and LNA together with non-eutectic formulations spanning several $LiNO_3$ mass fractions. Each composition was analyzed at least five times to ensure reproducibility.

Immediately after removal from the 110°C drying oven, 5–10 mg of powder was weighed to ±0.01 mg and sealed within 40-μL aluminum crucibles fitted with a vent pin no later than 1 min after weighing to minimize moisture uptake. DSC measurements were performed on a DSC 3+ (Mettler Toledo) under nitrogen flowing at 40 mL min^{-1}. The temperature was ramped from 30°C to 400°C at 20°C min^{-1}. Baseline linearity between 50°C and 300°C was confirmed following ISO 11357-1. A virtual baseline drawn between the extrapolated onset and end of the transition (endset), as specified by ISO 11357 and ASTM E794, was used for enthalpy integration.

In this study, the onset temperature was determined as the point where the extrapolated baseline intersects the leading edge of the endothermic peak in the DSC curve, while the endset temperature was identified where the baseline intersects the trailing edge of the peak. The latent heat was calculated by integrating the area under the heat-flow curve between these onset and endset temperatures.

A single heating rate was used to ensure consistent comparison with battery-durability protocols. Because the PCMs are intended for external placement, they were tested in sealed pans without electrolyte, isolating intrinsic phase-change behavior. This approach allowed us to focus on two critical parameters of the PCMs phase-change behavior: the onset temperature, where significant heat absorption begins, and the latent heat, which quantifies total heat-absorption capacity. By testing the PCMs in sealed aluminum crucibles without any additional materials, we isolated their inherent thermal characteristics under uniform heating conditions, ensuring the results reflect only the properties of the PCMs themselves.

The DSC instrument was calibrated using standard materials such as indium, zinc, and aluminum. The uncertainty in temperature measurement was maintained within ±0.2°C and the error in heat-flow rate was within ±2%. The thermal analysis results provided critical insights into the suitability of each PCM composition for battery thermal-management applications.

Table 4. Key hot-plate soak metrics for the LK90 PCM-HS

Metric	Value	Meaning
$t_{130,back}$	520 s	latency to reach lower safety limit
$t_{190,back}$	1,460 s	latency to reach upper safety limit
Minimum dT/dt inside window	−0.001°C s^{-1}	deepest part of latent valley
Dwell time t_{190}–t_{130}	940 s	duration inside safety window

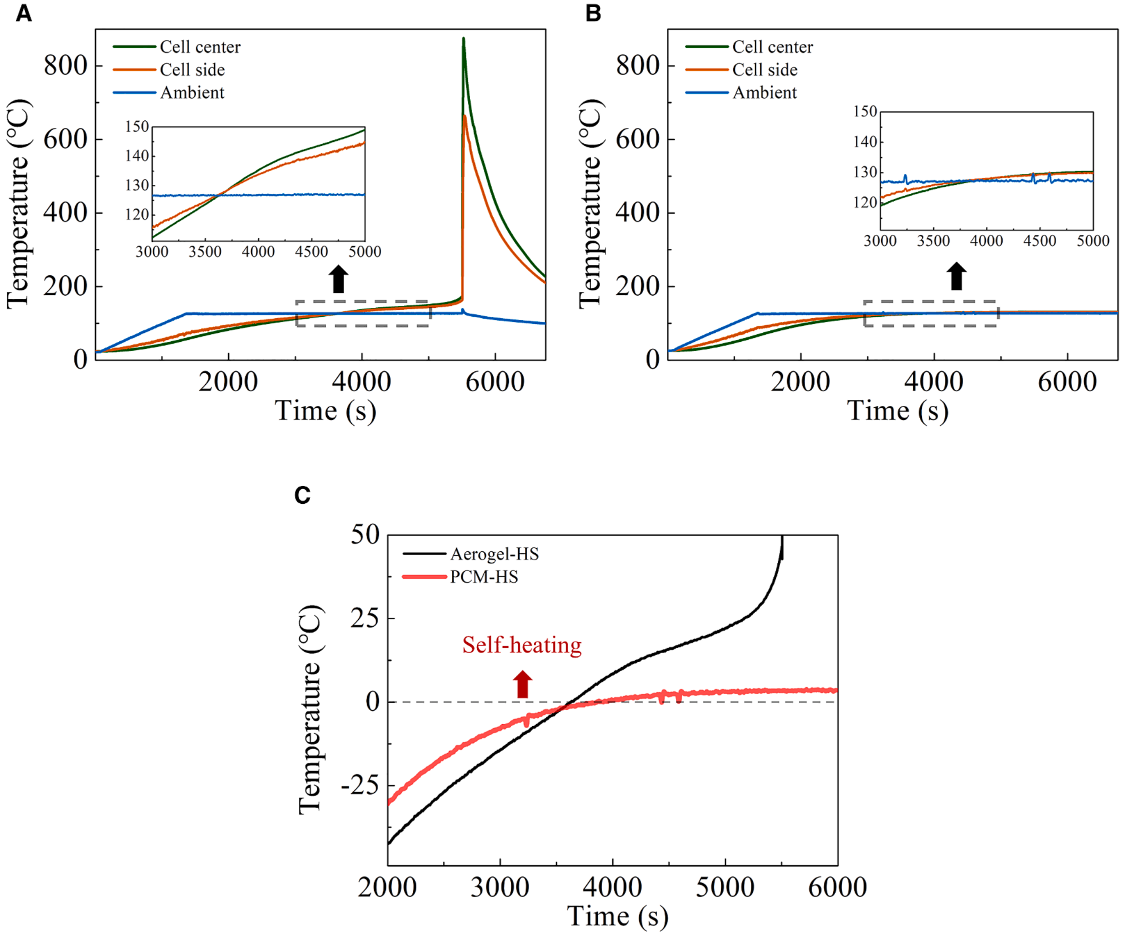

Figure 5. Thermal stability chamber test at 130°C

(A) Aerogel-HS: T_{center} (green) and T_{side} (orange) overtake $T_{ambient}$ (blue) and trigger TR at 5,506 s.

(B) PCM-HS: T_{center} and T_{side} remain near 131°C for the entire 90-min dwell without TR.

(C) Temperature excess, $\Delta T = T_{center}$-$T_{ambient}$. Aerogel-HS (black) rises into positive territory, signaling self-heating, while PCM-HS (red) peaks at 4°C then declines, confirming that latent melting suppresses internal heat generation.

Film-heater ramp test

A rapid-heating protocol that emulates the first seconds of battery ignition was designed to quantify the simultaneous heat absorption and rear-face heat shielding. A polyimide film heater, surface resistance 50 Ω, was bonded to the exposed face of each heat-shield specimen. The heater was driven in constant-voltage mode by a programmable supply UPL3000-5H (UNI). The supply started at 0 V and increased at 6 V min^{-1}, raising the electrical input by about 120 W min^{-1} and reproducing the characteristic power ramp of TR conditions without using a real battery cell.

Each specimen formed the core of a symmetric stack: aluminum plate, insulation board, film heater, heat shield, insulation board, aluminum plate. The insulation board, bulk conductivity near 0.1 W m^{-1} K^{-1}, confined heat flow through the shield. The stack was compressed to match the clamping pressure used in commercial EV battery modules.

Type-K thermocouples, wire diameter 0.5 mm, were soldered at the geometric centers of the front surface (TC1) and back surface (TC2). Signals were sampled at 10 Hz by a cDAQ-9174 (National Instruments) linked to LabVIEW. Raw temperatures were smoothed with a third-order Savitzky-Golay polynomial filter that used a 40-s symmetric window. A subsequent 10-s moving average removed residual high-frequency noise before differentiation.

Two heat shields were evaluated: the PCM-HS, thickness 3 mm, and an aerogel-HS of equal thickness. Every configuration was repeated three times. The largest run-to-run deviation in any temperature trace did not exceed ±5°C.

Figure 6B presents the full apparatus and the locations of TC1 and TC2. The processed data delivered the front-side and back-side temperature histories, their time derivatives, and the cumulative heat terms that appear in Table 3 of the results and discussion section.

Hot-plate dwell test

A constant-boundary experiment quantified the heat-absorption capacity of the PCM-HS under a steady flux. A laboratory

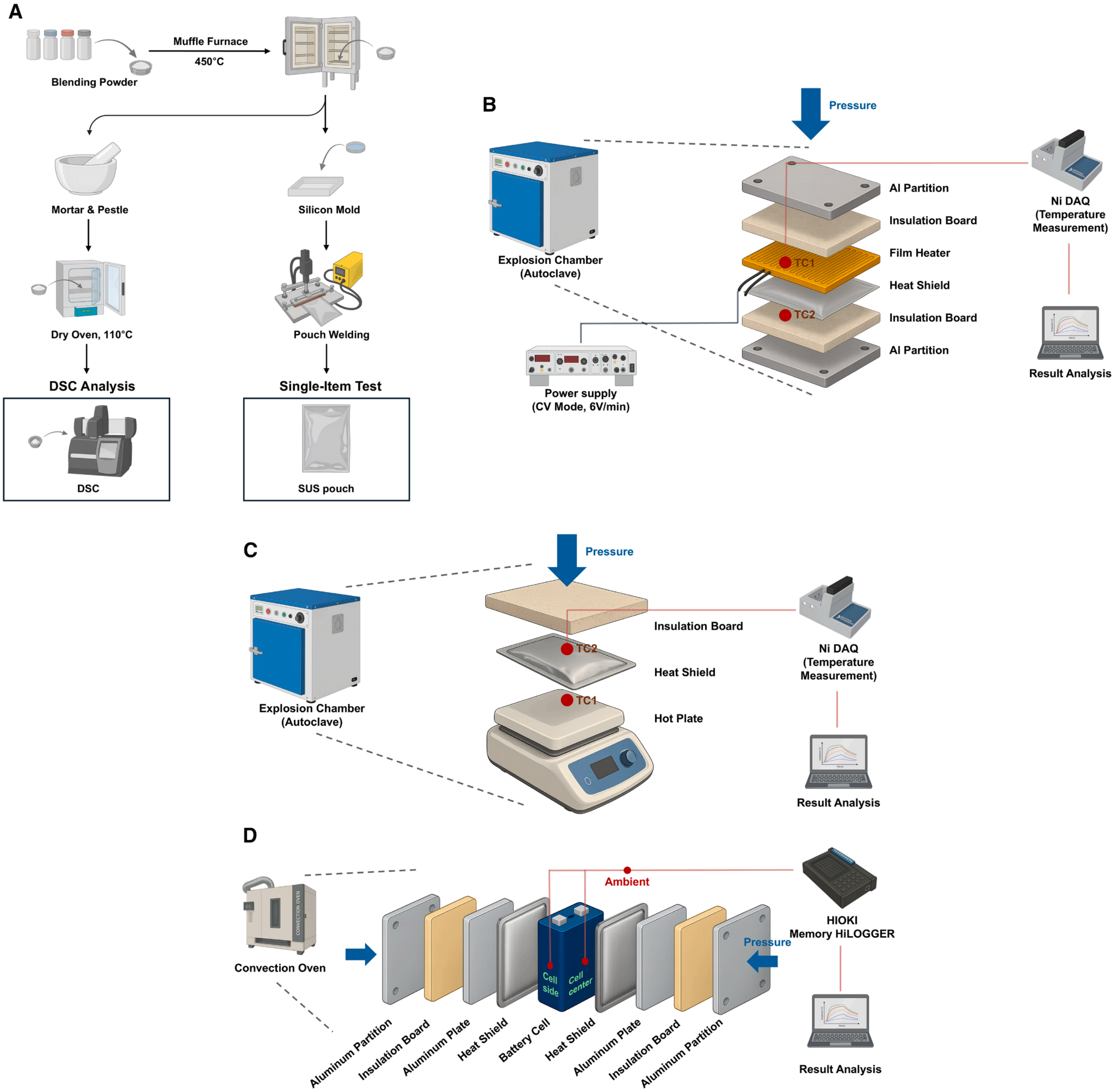

Figure 6. Preparation and experimental setups

(A) Preparation workflow for $LiNO_3$-based PCM-HSs: salt mixing, fusing, grinding, drying, casting, and pouch encapsulation.

(B) Film-heater ramp-test setup and thermocouple positions, showing aluminum plates, insulation boards, film heater, heat shields, and thermocouple placements.

(C) Hot-plate constant-temperature test setup for applying a 250°C boundary, with thermocouple positions on front and back faces of the PCM-HS.

(D) Thermal-stability oven-soak setup, including cell, PCM-HS or aerogel-HS, aluminum plates, insulation boards, and thermocouple positions.

hot plate DH.WHP04020 (DAIHAN Scientific, plate area 200 × 200 mm) was stabilized at 250°C and checked with a calibrated surface probe. The PCM-HS, thickness 3 mm, was placed flat on the plate and loaded with a 10-kg steel block to eliminate air gaps.

The measuring stack, from the plate upward, consisted of the hot-plate surface, the PCM-HS, and an insulation board of the same footprint. Two type-K thermocouples with 0.5-mm wire diameter were bonded using Kapton tape. One sensor was fixed at the geometric center of the interface between the plate and

PCM-HS and served as the front-side temperature. The other was attached at the center of the opposite face and served as the back-side temperature. Temperature signals were recorded at 10 Hz with a cDAQ 9174 (National Instruments) controlled by LabVIEW for a total of 40 min.

Raw temperatures were processed with a third-order Savitzky-Golay polynomial filter that used a symmetric window of 401 points. A subsequent 101-point moving average removed residual high-frequency noise. Back-side derivatives were then obtained by central differencing of the smoothed data.

Key metrics extracted were the times required for the back-side temperature to reach 130°C and 190°C, the minimum derivative within the 140°C–260°C latent-heat absorption interval determined from the DSC curve, and the dwell time between the two safety limits. All measurements were repeated three times, and the variation between runs did not exceed ±3°C.

Figure 6C shows the test assembly and the thermocouple positions.

Oven-soak thermal-stability test

This thermal-stability protocol drew its structure from IEC 62133-2 and UL 1642. Both standards expose lithium-ion cells to an oven that rises at 5°C min^{-1} until the air reaches 130°C ± 2°C. IEC62133-2 then holds the temperature for 30 min and UL 1642 holds for 10 min. This work extended the dwell to 90 min so that the full TR-management window between 130°C and 190°C could be probed. The aim was to compare a PCM-HS with an aerogel-HS and to determine which design maintains the cell below the separator melting threshold when every surrounding surface is fixed at 130°C.

Each specimen formed a symmetric stack. From the hot side to the cold side, the layers were an aluminum partition (100 × 80 × 10 mm), an insulation board (100 × 80 × 10 mm), an aluminum plate representing the face of a neighboring cell (100 × 80 × 10 mm), the heat shield (80 × 60 × 3 mm), a fully charged mini prismatic nickel-cobalt-aluminum oxide (NCA) cell (80 × 60 × 10 mm; nominal capacity 7.5 Ah; nominal voltage 4.2 V; nickel 90%), a second heat shield (80 × 60 × 3 mm), a second aluminum plate (100 × 80 × 10 mm), a second insulation board (100 × 80 × 10 mm), and a second aluminum partition (100 × 80 × 10 mm). The reference shield was a commercial silica aerogel-HS with a planform of 80 × 60 mm and thickness 3 mm. The comparison shield was a stainless-steel pouch containing the LK90 mixture with the same planform and thickness, which is PCM-HS. A constant mechanical clamp reproduced the compression found in production battery modules.

Three type-K thermocouples with wire diameter 0.5 mm were fixed with high-temperature ceramic adhesive. One probe touched the geometric center of the wide face of the cell. A second probe contacted the middle of the long edge of the cell. A third probe measured the oven air 10 mm above the specimen. Signals were recorded with a memory HiLOGGER (LR 8400, HIOKI) at 1 Hz with an accuracy of 1°C.

The convection oven (ENEX science) temperature increased at 5°C min^{-1} until it reached 130°C and then remained constant for 90 min. No current flowed in or out of the cell during the test. TR was declared when a vent rupture occurred. At that moment the oven power turned off and the specimen remained inside until its temperature fell below 50°C.

The recorded profiles of cell center temperature, cell side temperature, and ambient temperature were compared afterward. The difference between center and ambient temperatures served as the main indicator of self-heating and therefore of the capability of each heat shield to manage battery TR.

Figure 6D shows the stack assembly for the thermal-stability test.

RESOURCE AVAILABILITY

Lead contact

Requests for further information and resources should be directed to and will be fulfilled by the lead contact, Prof. Jack J. Yoh (jjyoh@snu.ac.kr).

Materials availability

The LK90 molten-salt PCM and PCM-HSs generated in this study are associated with a patent application in preparation and cannot be freely distributed. Requests for materials will be considered by the lead contact, and a materials transfer agreement may be required.

Data and code availability

- All data reported in this paper will be shared by the lead contact upon request.
- This paper does not report original code.
- Any additional information required to reanalyze the data reported in this paper is available from the lead contact upon request.

ACKNOWLEDGMENTS

The work was supported by Samsung SDI, contracted through IAAT and IOER at Seoul National University. Additional funding was provided from the US Air Force Office of Scientific Research under award number FA9550-24-1-0264.

AUTHOR CONTRIBUTIONS

Conceptualization, J.J.Y.; investigation, J.-Y.C. and M.-H.P.; data curation, J.-Y.C. and M.-H.P.; writing – original draft, J.-Y.C. and M.-H.P.; writing – review & editing, J.J.Y.; project administration, J.J.Y.; funding acquisition, J.J.Y.

DECLARATION OF INTERESTS

The authors declare that a patent application related to the LK90 molten-salt PCM and associated heat-shield technology is in preparation.

DECLARATION OF GENERATIVE AI AND AI-ASSISTED TECHNOLOGIES IN THE WRITING PROCESS

During the preparation of this work, the authors used ChatGPT (OpenAI) to improve clarity and readability of the text. After using this tool, the authors reviewed and edited the content as needed and take full responsibility for the content of the publication.

Received: June 17, 2025
Revised: September 14, 2025
Accepted: October 2, 2025
Published: October 30, 2025

REFERENCES

1. Bandhauer, T.M., Garimella, S., and Fuller, T.F. (2011). A Critical Review of Thermal Issues in Lithium-Ion Batteries. J. Electrochem. Soc. *158*, R1. https://doi.org/10.1149/1.3515880.

2. Wang, Q., Ping, P., Zhao, X., Chu, G., Sun, J., and Chen, C. (2012). Thermal runaway caused fire and explosion of lithium ion battery. J. Power Sources *208*, 210–224. https://doi.org/10.1016/j.jpowsour.2012.02.038.
3. Arora, S., Shen, W., and Kapoor, A. (2016). Review of mechanical design and strategic placement technique of a robust battery pack for electric vehicles. Renew. Sustain. Energy Rev. *60*, 1319–1331. https://doi.org/10.1016/j.rser.2016.03.013.
4. Feng, X., Ouyang, M., Liu, X., Lu, L., Xia, Y., and He, X. (2018). Thermal runaway mechanism of lithium ion battery for electric vehicles: A review. Energy Storage Mater. *10*, 246–267. https://doi.org/10.1016/j.ensm.2017.05.013.
5. Yang, S., Wang, W., Lin, C., Shen, W., and Li, Y. (2019). Investigation of internal short circuits of lithium-ion batteries under mechanical abusive conditions. Energies *12*, 1885. https://doi.org/10.3390/en12101885.
6. Zhang, S.S. (2007). A review on the separators of liquid electrolyte Li-ion batteries. J. Power Sources *164*, 351–364. https://doi.org/10.1016/j.jpowsour.2006.10.065.
7. Larsson, F., Andersson, P., Blomqvist, P., and Mellander, B.E. (2017). Toxic fluoride gas emissions from lithium-ion battery fires. Sci. Rep. *7*, 10018. https://doi.org/10.1038/s41598-017-09784-z.
8. Feng, X., Ren, D., He, X., and Ouyang, M. (2020). Mitigating Thermal Runaway of Lithium-Ion Batteries. Joule *4*, 743–770. https://doi.org/10.1016/j.joule.2020.02.010.
9. Golubkov, A.W., Fuchs, D., Wagner, J., Wiltsche, H., Stangl, C., Fauler, G., Voitic, G., Thaler, A., and Hacker, V. (2014). Thermal-runaway experiments on consumer Li-ion batteries with metal-oxide and olivin-type cathodes. RSC Adv. *4*, 3633–3642. https://doi.org/10.1039/c3ra45748f.
10. Bandhauer, T.M., and Garimella, S. (2013). Passive, internal thermal management system for batteries using microscale liquid-vapor phase change. Appl. Therm. Eng. *61*, 756–769. https://doi.org/10.1016/j.applthermaleng.2013.08.004.
11. Wang, Q., Mao, B., Stoliarov, S.I., and Sun, J. (2019). A review of lithium ion battery failure mechanisms and fire prevention strategies. Prog. Energy Combust. Sci. *73*, 95–131. https://doi.org/10.1016/j.pecs.2019.03.002.
12. Liu, B., Jia, Y., Yuan, C., Wang, L., Gao, X., Yin, S., and Xu, J. (2020). Safety issues and mechanisms of lithium-ion battery cell upon mechanical abusive loading: A review. Energy Storage Mater. *24*, 85–112. https://doi.org/10.1016/j.ensm.2019.06.036.
13. An, Z., Shi, T., Du, X., An, X., Zhang, D., and Bai, J. (2024). Experimental study on the internal short circuit and failure mechanism of lithium-ion batteries under mechanical abuse conditions. J. Energy Storage *89*, 111819. https://doi.org/10.1016/j.est.2024.111819.
14. Ren, D., Feng, X., Lu, L., Ouyang, M., Zheng, S., Li, J., and He, X. (2017). An electrochemical-thermal coupled overcharge-to-thermal-runaway model for lithium ion battery. J. Power Sources *364*, 328–340. https://doi.org/10.1016/j.jpowsour.2017.08.035.
15. Ohsaki, T., Kishi, T., Kuboki, T., Takami, N., Shimura, N., Sato, Y., Sekino, M., and Satoh, A. (2005). Overcharge reaction of lithium-ion batteries. J. Power Sources *146*, 97–100. https://doi.org/10.1016/j.jpowsour.2005.03.105.
16. Lopez, C.F., Jeevarajan, J.A., and Mukherjee, P.P. (2015). Characterization of Lithium-Ion Battery Thermal Abuse Behavior Using Experimental and Computational Analysis. J. Electrochem. Soc. *162*, A2163–A2173. https://doi.org/10.1149/2.0751510jes.
17. Wang, Z., Yang, H., Li, Y., Wang, G., and Wang, J. (2019). Thermal runaway and fire behaviors of large-scale lithium ion batteries with different heating methods. J. Hazard. Mater. *379*, 120730. https://doi.org/10.1016/j.jhazmat.2019.06.007.
18. Kim, M., and Yoh, J.J. (2025). An electrochemical theory for repurposing battery thermal runaway as a propulsion mechanism. J. Electroanal. Chem. *985*, 119087. https://doi.org/10.1016/j.jelechem.2025.119087.
19. Xu, B., Lee, J., Kwon, D., Kong, L., and Pecht, M. (2021). Mitigation strategies for Li-ion battery thermal runaway: A review. Renew. Sustain. Energy Rev. *150*, 111437. https://doi.org/10.1016/j.rser.2021.111437.
20. Ping, P., Wang, Q., Huang, P., Li, K., Sun, J., Kong, D., and Chen, C. (2015). Study of the fire behavior of high-energy lithium-ion batteries with full-scale burning test. J. Power Sources *285*, 80–89. https://doi.org/10.1016/j.jpowsour.2015.03.035.
21. Ouyang, D., Weng, J., Hu, J., Chen, M., Huang, Q., and Wang, J. (2019). Experimental investigation of thermal failure propagation in typical lithium-ion battery modules. Thermochim. Acta *676*, 205–213. https://doi.org/10.1016/j.tca.2019.05.002.
22. Orendorff, C.J., Lambert, T.N., Chavez, C.A., Bencomo, M., and Fenton, K.R. (2013). Polyester separators for lithium-ion cells: Improving thermal stability and abuse tolerance. Adv. Energy Mater. *3*, 314–320. https://doi.org/10.1002/aenm.201200292.
23. Lopez, C.F., Jeevarajan, J.A., and Mukherjee, P.P. (2015). Experimental Analysis of Thermal Runaway and Propagation in Lithium-Ion Battery Modules. J. Electrochem. Soc. *162*, A1905–A1915. https://doi.org/10.1149/2.0921509jes.
24. Börger, A., Mertens, J., and Wenzl, H. (2019). Thermal runaway and thermal runaway propagation in batteries: What do we talk about? J. Energy Storage *24*, 100649. https://doi.org/10.1016/j.est.2019.01.012.
25. Jia, L., Wang, D., Yin, T., Li, X., Li, L., Dai, Z., and Zheng, L. (2022). Experimental Study on Thermal-Induced Runaway in High Nickel Ternary Batteries. ACS Omega *7*, 14562–14570. https://doi.org/10.1021/acsomega.1c06495.
26. Liu, F., Wang, J., Yang, N., Wang, F., Chen, Y., Lu, D., Liu, H., Du, Q., Ren, X., and Shi, M. (2022). Experimental study on the alleviation of thermal runaway propagation from an overcharged lithium-ion battery module using different thermal insulation layers. Energy *257*, 124768. https://doi.org/10.1016/j.energy.2022.124768.
27. Luo, J., Zou, D., Wang, Y., Wang, S., and Huang, L. (2022). Battery thermal management systems (BTMs) based on phase change material (PCM): A comprehensive review. Chem. Eng. J. *430*, 132741. https://doi.org/10.1016/j.cej.2021.132741.
28. Pereira da Cunha, J., and Eames, P. (2016). Thermal energy storage for low and medium temperature applications using phase change materials - A review. Appl. Energy *177*, 227–238. https://doi.org/10.1016/j.apenergy.2016.05.097.
29. Ma, R., Qi, X., Feng, X., and Wu, W. (2025). Rapid Optimization of Thermal Runaway Propagation Inhibition in Composite Phase Change Material-Based Battery Module. IEEE Trans. Transp. Electrific. *11*, 1666–1679. https://doi.org/10.1109/TTE.2024.3409164.
30. Zhang, W., Liang, Z., Yin, X., and Ling, G. (2021). Avoiding thermal runaway propagation of lithium-ion battery modules by using hybrid phase change material and liquid cooling. Appl. Therm. Eng. *184*, 116380. https://doi.org/10.1016/j.applthermaleng.2020.116380.
31. Ji, W., Dang, Y., Yu, Y., Zhou, X., and Li, L. (2025). Combination of Phase Change Composite Material and Liquid-Cooled Plate Prevents Thermal Runaway Propagation of High-Specific-Energy Battery. Applied Sciences (Switzerland) *15*, 1274. https://doi.org/10.3390/app15031274.
32. Lv, Y., Liu, G., Zhang, G., and Yang, X. (2020). A novel thermal management structure using serpentine phase change material coupled with forced air convection for cylindrical battery modules. J. Power Sources *468*, 228398. https://doi.org/10.1016/j.jpowsour.2020.228398.
33. Huynh, V.T., Chang, K., and Lee, S.W. (2023). Numerical Investigation of the Thermal Performance of a Hybrid Phase Change Material and Forced Air Cooling System for a Three-Cell Lithium-Ion Battery Module. Energies *16*, 7967. https://doi.org/10.3390/en16247967.
34. Hu, J., Yao, Z., Chen, A., Xiao, C., Zhang, G., and Yang, X. (2025). High thermal-conductive phase change material by carbon fiber orientation for thermal management and energy conversion application. Appl. Therm. Eng. *265*, 125566. https://doi.org/10.1016/j.applthermaleng.2025.125566.

35. Xiong, F., Zhou, J., Jin, Y., Zhang, Z., Qin, M., Han, H., Shen, Z., Han, S., Geng, X., Jia, K., and Zou, R. (2024). Thermal shock protection with scalable heat-absorbing aerogels. Nat. Commun. *15*, 7125. https://doi.org/10.1038/s41467-024-51530-3.

36. Chen, Z., Shan, F., Cao, L., and Fang, G. (2012). Preparation and thermal properties of n-octadecane/molecular sieve composites as form-stable thermal energy storage materials for buildings. Energy Build. *49*, 423–428. https://doi.org/10.1016/j.enbuild.2012.02.035.

37. Myers, P.D., and Goswami, D.Y. (2016). Thermal energy storage using chloride salts and their eutectics. Appl. Therm. Eng. *109*, 889–900. https://doi.org/10.1016/j.applthermaleng.2016.07.046.

38. Jiang, Y., Sun, Y., Bruno, F., and Li, S. (2017). Thermal stability of Na2CO3-Li2CO3 as a high temperature phase change material for thermal energy storage. Thermochim. Acta *650*, 88–94. https://doi.org/10.1016/j.tca.2017.01.002.

39. Orozco, M.A., Acurio, K., Vásquez-Aza, F., Martínez-Gómez, J., and Chico-Proano, A. (2021). Thermal storage of nitrate salts as phase change materials (PCMs). Materials *14*, 7223. https://doi.org/10.3390/ma14237223.

40. Alario, J., Kosson, R., and Haslett, R. (1980). Active heat exchange system development for latent heat thermal energy storage.

41. Gasanaliev, A.M., and Gamataeva, B.Y. (2000). Heat-accumulation properties of melts. Usp. Khim. *69*, 199–200. https://doi.org/10.1070/rc2000v069n02abeh000490.

42. Huang, Z., Gao, X., Xu, T., Fang, Y., and Zhang, Z. (2014). Thermal property measurement and heat storage analysis of LiNO3/KCl - expanded graphite composite phase change material. Appl. Energy *115*, 265–271. https://doi.org/10.1016/j.apenergy.2013.11.019.

43. Li, Y., Tie, W.C., Zhu, Q.Z., and Qiu, Z.Z. (2021). A Study of LiNO3–NaCl/EG Composite PCM for Latent Heat Storage. Int. J. Thermophys. *42*, 155. https://doi.org/10.1007/s10765-021-02908-8.

44. Li, Y., Yue, G., Yu, Y.M., and Zhu, Q.Z. (2020). Preparation and thermal characterization of LiNO3–NaNO3–KCl ternary mixture and LiNO3–NaNO3–KCl/EG composites. Energy *196*, 117067. https://doi.org/10.1016/j.energy.2020.117067.

45. Weng, J., Huang, Q., Li, X., Zhang, G., Ouyang, D., Chen, M., Yuen, A.C.Y., Li, A., Lee, E.W.M., Yang, W., et al. (2022). Safety issue on PCM-based battery thermal management: Material thermal stability and system hazard mitigation. Energy Storage Mater. *53*, 580–612. https://doi.org/10.1016/j.ensm.2022.09.007.